# Synthesis of layered 2H−MoSe$_2$ nanosheets for the high-performance supercapacitor electrode material

Sanjay Upadhyay, O.P. Pandey[*]

School of Physics and Materials Science, Thapar Institute of Engineering & Technology, Patiala, 147004, India

## ARTICLE INFO

## ABSTRACT

In this work, we report the synthesis of layered 2H−MoSe$_2$ nanosheets via an in-situ selenization route and investigated their electrochemical charge storage performance. The structure and morphology of the as-synthesized samples have been investigated systematically. The electrochemical performance of the MoSe$_2$ nanosheets towards the supercapacitor has been probed by a three-electrode cell configuration in 2 M KOH electrolyte solution. The prepared MoSe$_2$ nanosheets show excellent electrochemical performance with a specific capacity of 46.22 mAh g$^{-1}$ at a current density of 2 Ag$^{-1}$. The MoSe$_2$ electrode exhibit remarkable cyclic stability up to 2000 charge-discharge cycles. In addition, the fabricated MoSe$_2$ symmetric supercapacitor delivered a specific capacitance of 4.1 Fg$^{-1}$ at a current density of 0.5 Ag$^{-1}$. It exhibited high cyclic stability with capacitance retention of 105% and high coulombic efficiency of 100% even after 10000 cycles. The high specific capacity and good cyclic stability of the MoSe$_2$ nanosheets suggest its application as an efficient electrode material for electrochemical supercapacitor.

## 1. Introduction

The ever-increasing energy crisis and environmental pollution demand clean and renewable energy devices. The supercapacitor, which is also known as electrochemical supercapacitor or ultra-capacitor (ECs), can be a promising candidate for energy storage devices between conventional batteries and capacitors. They exhibit high power density, high reliability, high cyclic stability, and very short charging time [1,2]. However, the energy density of the supercapacitors is very much lower than that of commercial lithium-ion batteries to date, which restricted their industrial applications [3,4]. There are two types of ECs based on their charge storage mechanism (i) pseudocapacitors, which involves near-surface redox reactions of charged species with the electrode material, and (ii) double-layer capacitors, which store energy electrostatically through adoption/desorption of electrolyte ions on the electrolyte surface. Carbon-based materials such as carbon nanotubes [5], activated carbon [6−8], and graphene [9−11] were found as the best electrode materials for electric double-layer capacitors. However, they suffer from low energy density which is unfavorable for ECs. To encounter this problem a variety of pseudocapacitor

materials were investigated such as transition metal oxides (TMOs), conducting polymers, and transition metal dichalcogenides (TMDs). Among these materials conducting polymers and TMOs suffer from low cyclic stability and low electric conductivity respectively due to which they exhibit low electrochemical performance.

Nowadays, TMDs are under investigation extensively due to their 2D sheet-like morphology, high conductivity, high specific surface area, and variable oxidation states [12−14]. The structure of TMDs is analogous to graphene (layered structure) with the general formula MX$_2$ (M is a metal from groups 4 to 10 and X is a chalcogen such as S, Te, or Se). These layers are stacked together by weak vander Waals forces. The exfoliation of TMDs into monolayer or few layers from their bulk counterparts, which preserves their bulk properties, exhibits distinct chemical and physical properties. Therefore, they offer a range of applications in electronic devices, electro/photo catalysis, and electrochemical energy storage devices [15−18]. Among them, molybdenum selenides (MoS$_2$) was first reported in 2007 for electrochemical double-layer capacitance material by Soon and Loh [19]. There has been very little study of selenides compared to sulfides for electrochemical supercapacitors. MoSe$_2$ has a similar layered structure and has a higher electrical conductivity than MoS$_2$ due to the greater metallic nature of Se [20]. Fig. 1 represents the structure of a monolayer of MoSe$_2$ nanosheet which provides a large surface area and hence exhibits

* Corresponding author.
E-mail address: oppandey@thapar.edu (O.P. Pandey).

*S. Upadhyay and O.P. Pandey*
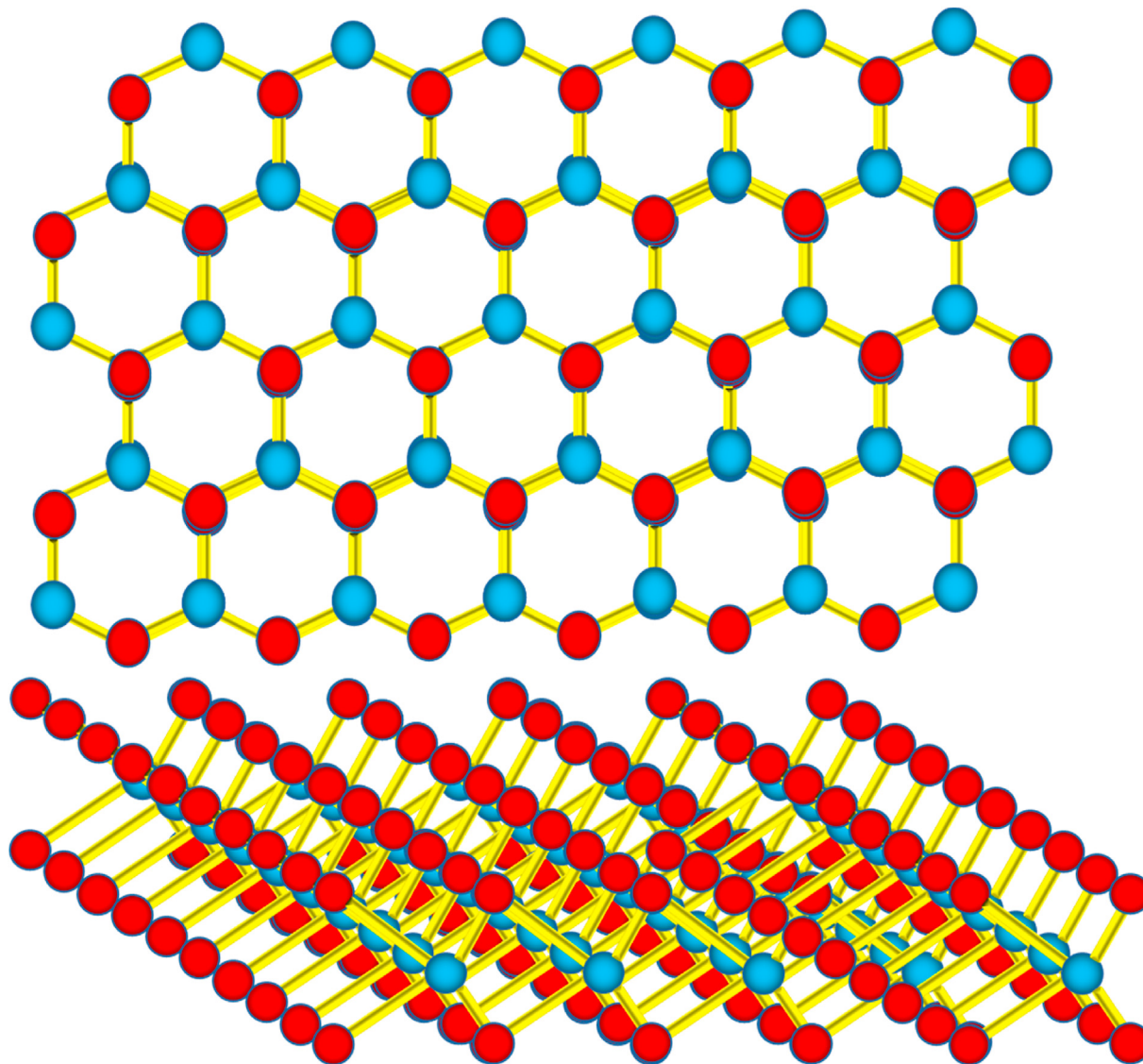
**Fig. 1.** Crystal Structure of monolayer of hexagonal MoSe$_2$ showing a layer of molybdenum atoms (blue) sandwiched between two layers of selenium atoms (red). (For interpretation of the references to colour in this figure legend, the reader is referred to the Web version of this article.)

high electrochemical performance. MoSe$_2$ has a high theoretical capacity and a bandgap of 1.5 eV which has been investigated for supercapacitor electrode material [21–23]. Also, the relatively larger interlayer spacing in MoSe$_2$ helps the ions to intercalate and extract higher current from the layered structure which makes it a better candidate as a supercapacitor electrode [24].

Intensive efforts have been made to synthesize highly efficient MoSe$_2$ powder via different synthesis routes. Balasingam et al. reported few-layered MoSe$_2$ nanosheets synthesized via a simple hydrothermal method which showed a high specific capacitance of 198.9 Fg$^{-1}$ at a scan rate of 2 mVs$^{-1}$ and high cyclic stability in 0.5 M H$_2$SO$_4$ [22]. Gao et al. synthesized MoSe$_2$ having spherical features using a facile hydrothermal route. These MoSe$_2$ spheres exhibited a large specific capacitance of 243 Fg$^{-1}$ at a current density of 0.5 Ag$^{-1}$ and kept its capacitance to 90.3% after 1000 cycles at 1Ag$^{-1}$ [23]. Jinbing Cheng and his group synthesized mesoporous MoSe$_2$ nanomaterials prepared by a simple and cost-effective hydrothermal method. The synthesized material exhibited a specific capacitance of 133 Fg$^{-1}$ at 2 Ag$^{-1}$ and maintained the primary capacitance to 95% over 2000 cycles [25]. Yongseok Jun group

synthesized MoSe$_2$/rGO nanosheets via a hydrothermal process which showed a specific capacitance of 211 Fg$^{-1}$ at a scan rate of 5 mVs$^{-1}$ however, the specific capacitance drops to 100 Fg$^{-1}$ when the scan rate rises to 125 mVs$^{-1}$ [26]. Pazhamalai et al. successfully synthesized 2H–MoSe$_2$ nanosheets through a hydrothermal method. The MoSe$_2$ symmetric supercapacitor (SSC) achieved a specific capacitance of 25.31 F g$^{-1}$ at a scan rate of 5 mV s$^{-1}$ [27]. Li et al. prepared MoSe$_2$/MWCNT composite for the supercapacitor application. The MoSe$_2$/MWCNT delivered a specific capacitance of 927.25 F g$^{-1}$ at a current density of 1 A g$^{-1}$ [28].

Generally, CVD, hydrothermal, or rapid thermal processing method is used to synthesize MoSe$_2$ nanosheets which are very complex and expensive for the synthesis at a large scale. The MoSe$_2$ nanosheets synthesized by the above-mentioned methods still suffer from low specific capacitance and hence they cannot be adopted for practical applications. To the best of our knowledge, no report deals with the synthesis of pure phase MoSe$_2$ nanosheets in a stainless-steel autoclave without an inert atmosphere. Moreover, the synthesis mechanism and the influence of reaction parameters on the phase formation of MoSe$_2$ has not been clearly understood

yet.

In this work, we report a facile, scalable, and cost-effective approach to synthesize layered MoSe$_2$ nanosheets via the in-situ selenization route for its application as an electrochemical supercapacitor electrode. The effect of reaction parameters on the phase formation has been studied in detail. The synthesized MoSe$_2$ nanosheets exhibit stacked plates structure and porous network which, facilitate fast charge transport and showed higher electrochemical reaction kinetics and hence exhibit high specific capacity. The MoSe$_2$ nanosheets showed a specific capacity of 46.22 mAh g$^{-1}$ at a current density of 2 A g$^{-1}$. The prepared nanosheets exhibit long-term stability and high coulombic efficiency up to 2000 GCD cycles at a current density of 5 Ag$^{-1}$. Also, the MoSe$_2$ symmetric supercapacitor (SSC) delivered a specific capacitance of 4.1 Fg$^{-1}$ at a current density of 0.5 Ag$^{-1}$ with outstanding cyclic performance and high coulombic efficiency up to 10000 cycles. The results in the present work suggest that the synthesis method reported here has the potential to fabricate highly efficient layered MoSe$_2$ nanosheets for high-performance electrochemical supercapacitors at a very low cost.

## 2. Experimental section

### 2.1. Preparation of MoSe$_2$ nanosheets

To obtain pure phase MoSe$_2$ powder, 0.3 g of (NH$_4$)$_6$Mo$_7$O$_{24}$·4H$_2$O, 1 g of Se, and 1 g of Mg metal powders were weighed and mixed in an agate mortar properly. The uniformly mixed powder was then transferred into a stainless-steel autoclave and sealed tightly. The autoclave was then heated in a pot furnace by raising the temperature to 800 °C from room temperature for 4 h. After cooling the autoclave naturally to room temperature, the gray powder was collected. The powder was then washed with (10:7) dilute hydrochloric acid (HCL) to remove Mg and MgO. The powder was then again washed with distilled water many times to take out HCL and was then dried at 110 °C in a hot air oven. The information about the reaction parameters and phases obtained are given in Table 1.

### 2.2. Characterization

The as-synthesized samples were probed by XRD for structural and phase analysis using a PANalytical X-Pert-Pro diffractometer with CuKα radiation (λ = 1.5406 Å) by a copper target in which Nickel filter was inbuilt. To get information about the morphological and microstructural properties, a scanning electron microscope (JEOL JSM-6510) and field emission scanning electron microscope (JEOL JSM 5600) operating at 15 kV were used. Also, a transmission electron microscope (JEOL 2100F) operating at 200 kV was used. X-ray photoelectron spectroscopy analysis was done using AlKα (1486.6 eV) radiation operating at 15 mA and 15 kV. The layers were

quantified by Raman spectroscopy via Jobin Yvon Horibra LABRAM-HR 800 (473 nm) at room temperature. Brunauer-Emmett-Teller (BET) measurements were evaluated to investigate the specific surface area and pore size distribution using a Quantachrome Instrument version 11.05 (Nova Station A) in a nitrogen (N$_2$) atmosphere.

### 2.3. Electrochemical measurements

All the electrochemical measurements were performed in a three-electrode cell configuration using a biologic EC lab SP300 standard setup in 2 M KOH electrolyte solution. In the process of preparing the working electrode, the as-synthesized MoSe$_2$ nanosheets, carbon black, and Nafion 117 solution (Sigma Aldrich) in a mass ratio of 80:15:5 were mixed to make a slurry. The slurry was diluted by mixing ethanol in such a way that it can be dropwise coated onto a 1 cm$^2$ nickel foam. The mass loading of MoSe$_2$ on the Ni foam was 1 mg. The coated nickel foam was then dried at 60 °C for 8 h in a hot air oven. The platinum electrode and saturated calomel electrode (SHE) were used as counter and reference electrodes respectively. Firstly, 30 cyclic voltammetry (CV) cycles were performed at a scan rate of 100 mVs$^{-1}$ within a potential range of +1 to −1 V to activate the surface. It also helps to stabilize the electrochemical currents and remove the contamination from the electrode surface [29]. After that, the CV measurements were performed at various scan rates ranging from 5 to 125 mVs$^{-1}$ in a voltage window of 0−0.4 V. The galvanic charge-discharge curves were measured at different current densities ranging from 2 to 10 Ag$^{-1}$ in the same voltage range as used in the CV measurements. Also, electrochemical impedance spectroscopy (EIS) was performed over the frequency range of 10$^2$−10$^{-2}$ kH$_z$ at various AC amplitudes ranging from 100 to 800 mV.

### 2.3.1. SSC fabrication and calculation

To fabricate the MoSe$_2$ SSC, two Ni-foams having a geometric area of 1 cm$^2$ each, were coated with MoSe$_2$ powder with the same procedure as mentioned above. The mass loading of MoSe$_2$ per electrode was 1 mg and the ratio of MoSe$_2$, carbon black and Nafion 117 solution in the slurry was 80:15:5. A 2M-KOH soaked Whatman paper was used as a separator for SSC.

The specific capacity was calculated from the GCD measurements using the following equation:

$$C_{sp} = \frac{I \triangle t}{m} \tag{1}$$

where C$_{sp}$ is the specific capacity (mAh g$^{-1}$), I is the applied current (A), Δt is the discharge time (s) and m is the mass of the electrode active material (g).

The specific capacitance of the MoSe$_2$ SSC was calculated using the following equation:

**Table 1**
Reaction parameters, major and minor phases obtained, and crystallite size.

| S. No. | Temperature (°C) | Holding time (h) | Molar ratio of precursors (Mo:Se) | Phases obtained | | Crystallite Size (nm) |
|---|---|---|---|---|---|---|
| | | | | Major | Minor | |
| 1 | 700 | 4 | 1:49 | MoSe$_2$ | Se, Mo | 31.90 |
| 2 | 800 | 4 | 1:49 | MoSe$_2$ | — | 40.70 |
| 3 | 800 | 3 | 1:49 | MoSe$_2$ | Mo$_3$Se$_4$, Mo, Se | 29.40 |
| 4 | 800 | 5 | 1:49 | MoSe$_2$ | Se, Mo | 27.45 |
| 5 | 800 | 4 | 1:39 | MoSe$_2$ | Mo$_3$Se$_4$, Mo, Se | 29.34 |
| 6 | 800 | 4 | 1:59 | MoSe$_2$ | Se | 36.11 |

S. Upadhyay and O.P. Pandey

$$C_s = \frac{2I\triangle t}{m\triangle V} \qquad (2)$$

Here $C_s$ is the specific capacitance (Fg$^{-1}$), m is the mass of one electrode (g) and $\Delta V$ is the potential window (V).

The Energy density "E" (Wh Kg$^{-1}$) and power density "P" (W kg$^{-1}$) of the MoSe$_2$ SSC was calculated from the following equations:

$$E = \frac{C_s \Delta V^2}{8} \qquad (3)$$

$$P = \frac{E}{\Delta t} \qquad (4)$$

## 3. Results and discussion

### 3.1. XRD

The phase and structural investigations of the samples were done using the XRD technique. The X-ray diffraction pattern of the MoSe$_2$ powder synthesized at a reaction temperature of 800 °C for 4 h is shown in Fig. 2. The peaks having 2θ values 13.8, 27.6, 31.4, 34.4, 38.0, 42.0, 47.4, 53.4, 55.9, 56.9, 57.9, 66.6, 69.5, 71.8, 72.1, 76.2 and 83.8 were observed, which corresponds to single-phase 2H−MoSe$_2$ (ICDD card number- 00-029-0914). The XRD analysis revealed that the 2H−MoSe$_2$ powder is crystalline with a hexagonal structure. Here, the absence of any peak other than MoSe$_2$ in the XRD pattern indicates the formation of pure phase MoSe$_2$. The results are in good agreement with the reduction of MoO$_3$ to form MoSe$_2$ in presence of reducing agent magnesium (Mg) and high pressure generated inside the autoclave. Mg helps in the reduction of MoO$_3$ and MoO$_2$ to Mo metal, leaving MgO and unreacted Mg as byproducts. Moreover, the washing of the prepared sample with

diluted HCl removes only unwanted MgO and unreacted Mg from the prepared sample in the following manner [30,31].

$$Mg + 2HCl \rightarrow MgCl_2 + H_2 \qquad (5)$$

$$MgO + 2HCl \rightarrow MgCl_2 + H_2O \qquad (6)$$

The results obtained are in good agreement with the reported literature that there is no phase change before and after the HCl etching. However, it washes out only Mg and MgO from the sample leaving behind the final product of pure MoSe$_2$ [32−34]. Therefore, no peak corresponding to the oxide phases is present in the XRD pattern. The crystallite size was calculated to be equal to 40.7 nm using the Debye Scherrer equation,

$$D_{hkl} = \frac{0.9\lambda}{\beta_{hkl} \, cos\theta} \qquad (7)$$

where λ is the wavelength of the X-ray, $\beta_{hkl}$ is the FWHM, and θ is the diffraction angle.

To understand the effect of reaction parameters on the phase formation, a series of experiments were done at the different reaction temperature, time, and molar ratio of precursors. In Fig. S1 (SI), the XRD patterns of the powders synthesized at different reaction temperatures at a constant reaction time of 4 h and the molar ratio of 1:49 (Mo:Se) are shown. Fig. S1a (SI) shows the XRD pattern of the sample synthesized at 700 °C. At this temperature, MoSe$_2$ along with unreacted Se and Mo were found with a vol% of 81.89, 7.87, and 10.24 respectively. It indicates that this temperature was not sufficient enough to react Mo and Se completely to form MoSe$_2$. The Se and Mo peaks can be matched with ICDD card no. (01-073-0465) and (01-089-5023) respectively. Further raising the reaction temperature to 800 °C, single-phase MoSe$_2$ was obtained (Fig. S1b, SI). The crystallite size increases with reaction temperature from 31.9 nm at 700 °C to 40.7 nm at 800 °C. Due to the ordered structure the crystallite size increases. Above 700 °C, the
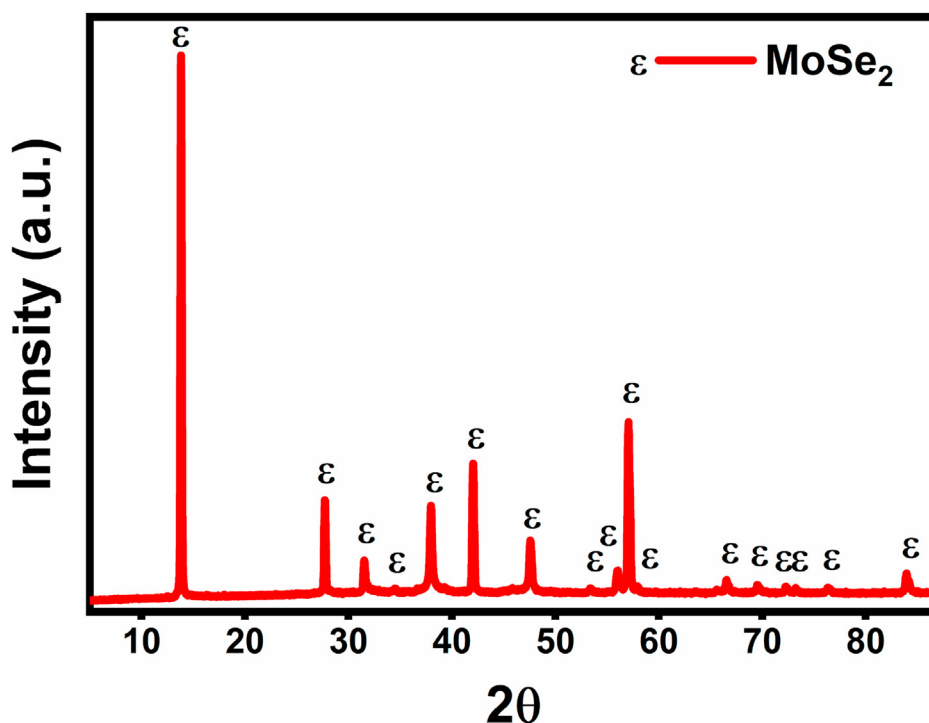


Fig. 2. XRD pattern of the as-synthesized MoSe$_2$ powder.
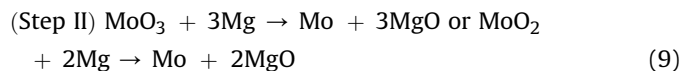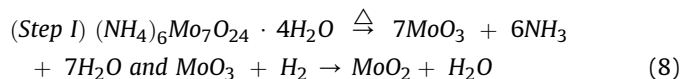
*S. Upadhyay and O.P. Pandey*

unreacted Se and Mo forms highly ordered pure phase $MoSe_2$ powder, and hence the crystallite size increases.

In the second set of experiments, the variation in reaction time was done at a constant reaction temperature of 800 °C and molar ratio of 1:49 (Mo:Se). The XRD patterns of the synthesized samples are shown in Fig. S2 (SI). At 3 h of reaction time, the peaks corresponding to $MoSe_2$, $Mo_3Se_4$ (ICDD card no. 01-085-0455), Mo, and Se were obtained with a vol% of 67.13, 2.98, 6.09, and 23.80 respectively (Fig. S2a, SI). This shows that the reaction time was not sufficient for Mo and Se to react completely. However, the pure phase $MoSe_2$ was obtained at 4 h of reaction time (Fig. S2b, SI). Further increasing the reaction time to 5 h, the peaks corresponding to $MoSe_2$ (81.68 vol%), Mo (7.34 vol%), and Se (10.98 vol%) were observed (Fig. S2c, SI). It indicates the decomposition of $MoSe_2$ to Mo and Se. The crystallite size first increases from 29.4 nm at 3 h to 40.7 nm at 4 h and then decreases to 27.45 nm at 5 h of reaction time. When the reaction time was increased from 3 h to 4 h, the $Mo_3Se_4$, Mo, and Se transforms into ordered $MoSe_2$ powder, and hence the crystallite size increases. However, above 4 h of reaction time, the bonds inside $MoSe_2$ break, and the order inside the powder decreases, and hence the crystallite size decreases.

In the third set of experiments, the variation in the molar ratio of the precursors was done at a constant reaction temperature of 800 °C and a reaction time of 4 h. Fig. S3 (SI) shows the XRD patterns of the samples synthesized at various molar ratios of precursors. At a molar ratio of 1:39 (Mo:Se), the characteristic peaks of $MoSe_2$ (83.14 vol%), $Mo_3Se_4$ (6.84 vol%), Mo (5.35 vol%), and Se (4.67 vol%) were observed (Fig. S3a, SI). As discussed earlier, single-phase $MoSe_2$ was obtained at a molar ratio of 1:49 (Fig. S3b, SI). The powders synthesized at 1:59 (Mo:Se) was composed of $MoSe_2$ and Se with a vol% of 98.15 and 1.85 (Fig. S3c). The presence of Se in the XRD pattern indicates that the amount of Se source was higher than the required amount for the formation of pure phase $MoSe_2$ and hence remain unreacted. The variation in crystallite size with the molar ratio of precursors shows similar behavior to that observed at different reaction times. First, it increases with increasing molar ratio of precursors and then decreases. The crystallite size of the powders synthesized at a molar ratio of 1:39, 1:49, and 1:59 was calculated to be equal to 29.34, 40.70, and 36.11 nm respectively. When the molar ratio increases from 1:39 to 1:49, highly ordered $MoSe_2$ is formed by the transformation of $Mo_3Se_4$, Mo, and Se, and hence the crystallite size increases. However, when the molar ratio increases from 1:49 to 1:59, extra Se decreases the order inside the powder, and hence the crystallite size decreases.

All the above results indicate that the formation of pure phase $MoSe_2$ is a very critical process and has a very narrow window. And pure phase $MoSe_2$ can be obtained at a particular reaction temperature, reaction time, and molar ratio of precursors. Depending upon the aforementioned experimental outcomes, the probable redox reactions involved in the autoclave synthesis of $MoSe_2$ can be expressed in three steps as follows.

In the first step, AHM decomposes to $MoO_3$ at high temperatures, and $MoO_3$ can reduce to $MoO_2$ in the presence of $N_2/H_2$ or $NH_3$. In the second step, the obtained $MoO_3$ or $MoO_2$ reduces to Mo metal with the help of a reducing agent [35]. In this work, Mg was used as a reducing agent which reduces $MoO_3$ and $MoO_2$ to Mo [36]. Mg is a highly reactive substance and hence it acts as a catalyst. Further, it reacts with the oxygen present in the autoclave and forms MgO, which also acts as a catalyst. MgO reduces the gaseous compounds into carbon and hydrogen, which helps in the reduction of $MoO_3$ and $MoO_2$ to Mo [34]. Also, it absorbs oxygen from the autoclave, which hinders the conversion of $MoSe_2$ to $MoO_3$. In the final step, Se metal reacts with Mo metal to produce $MoSe_2$.

$$(Step\ I)\ (NH_4)_6Mo_7O_{24} \cdot 4H_2O \xrightarrow{\triangle} 7MoO_3 + 6NH_3$$
$$+ 7H_2O\ and\ MoO_3 + H_2 \rightarrow MoO_2 + H_2O \tag{8}$$

$$(Step\ II)\ MoO_3 + 3Mg \rightarrow Mo + 3MgO\ or\ MoO_2$$
$$+ 2Mg \rightarrow Mo + 2MgO \tag{9}$$

$$(Step\ III)Mo + 2Se \rightarrow MoSe_2 \tag{10}$$

### 3.2. XPS

The chemical composition of the as-synthesized $MoSe_2$ powder was investigated by X-ray photoelectron spectroscopy (XPS) measurements (Fig. 3). The survey spectrum is shown in Fig. 3a, which indicates the presence of Mo, Se, and O elements within the sample. The deconvolution of the high-resolution spectrum of Mo 3d shows four peaks. The peaks at 232.1 and 232.7 eV can be assigned to Mo $3d_{3/2}$ and the other two peaks at 228.9 and 229.6 eV can be assigned to Mo $3d_{5/2}$ (Fig. 3b) [37–39]. The high-resolution spectra of O1s can be divided into five peaks positioned at 530.5, 531.6, 532.4, 533, and 534.1 eV which are related to C=O, C–O–Mo, C–O, C–OH, and O–C=O respectively (Fig. 3c) [40–42]. The presence of C and O elements may be due to the exposure of the sample surface to air.

### 3.3. SEM and FESEM

The morphology of the synthesized $MoSe_2$ powder was investigated using scanning electron microscopy (SEM). Fig. 4 shows the SEM micrographs of the $MoSe_2$ powder. The continuous sheet network having porosity can be observed in Fig. 4a. These sheets have different sizes as shown in Fig. 4b. Fig. 4c demonstrates that these sheets involve porosity of the order of few micrometers (1–2 μm). The porous sheets may help to improve the electrochemical capacitance of the $MoSe_2$ powder. The overall features of the $MoSe_2$ powder can be observed in Fig. 4d. Fig. 4e reveals the presence of layered microspheres as well as hexagonal sheet structures on the surface of the $MoSe_2$ network. The layered microspheres provide a large surface area and hence improves the electrochemical performance. The field emission scanning electron microscopy (FESEM) was also employed on the sample to get more information about the morphological structure. Fig. 5 shows the FESEM micrographs of the as-prepared $MoSe_2$ powder. The stacked plates structure can be seen in Fig. 5a as expected for $MoSe_2$. This type of structure plays a crucial role in the electrochemical properties of the material. It helps to improve the electrochemical capacitance of the electrode material. The hexagonal-shaped structure shown in Fig. 5b further confirms the presence of hexagonal structure. In addition, the FESEM results revealed that there is no clear uniform morphology present within the sample. The agglomeration of uneven particles can also be observed. The elemental analysis was done by EDS measurements which confirms the presence of Mo and Se elements within the sample (Fig. 5d). Table 2 represents the weight and atomic percentages calculated from EDS measurements.

### 3.4. TEM

Transmission electron microscopy (TEM) was done to investigate the microstructure of the synthesized $MoSe_2$ powder and the micrographs are shown in Fig. 6. The micrographs clearly show the
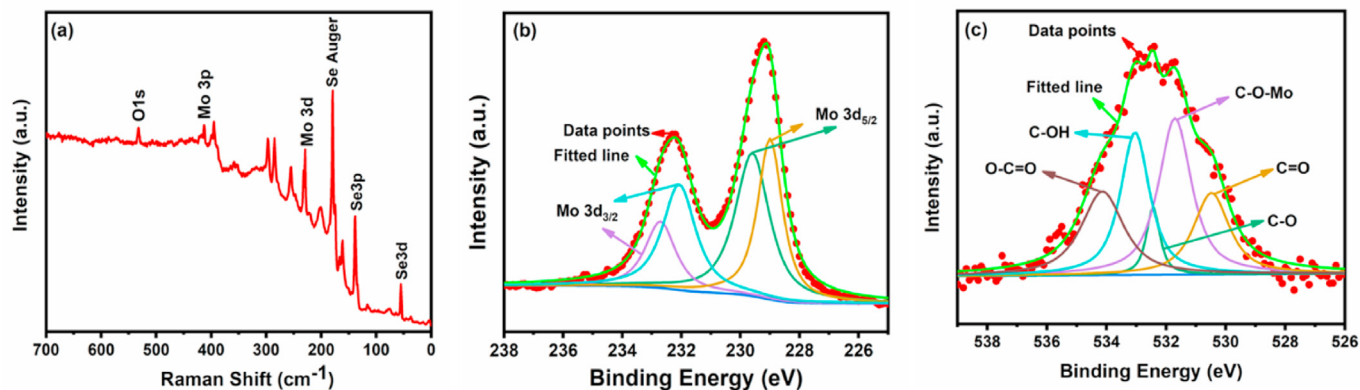
S. Upadhyay and O.P. Pandey

**Fig. 3.** (a) XPS survey spectra (b) high resolution Mo3d spectra and (c) high resolution O1s spectra of MoSe$_2$ powder.
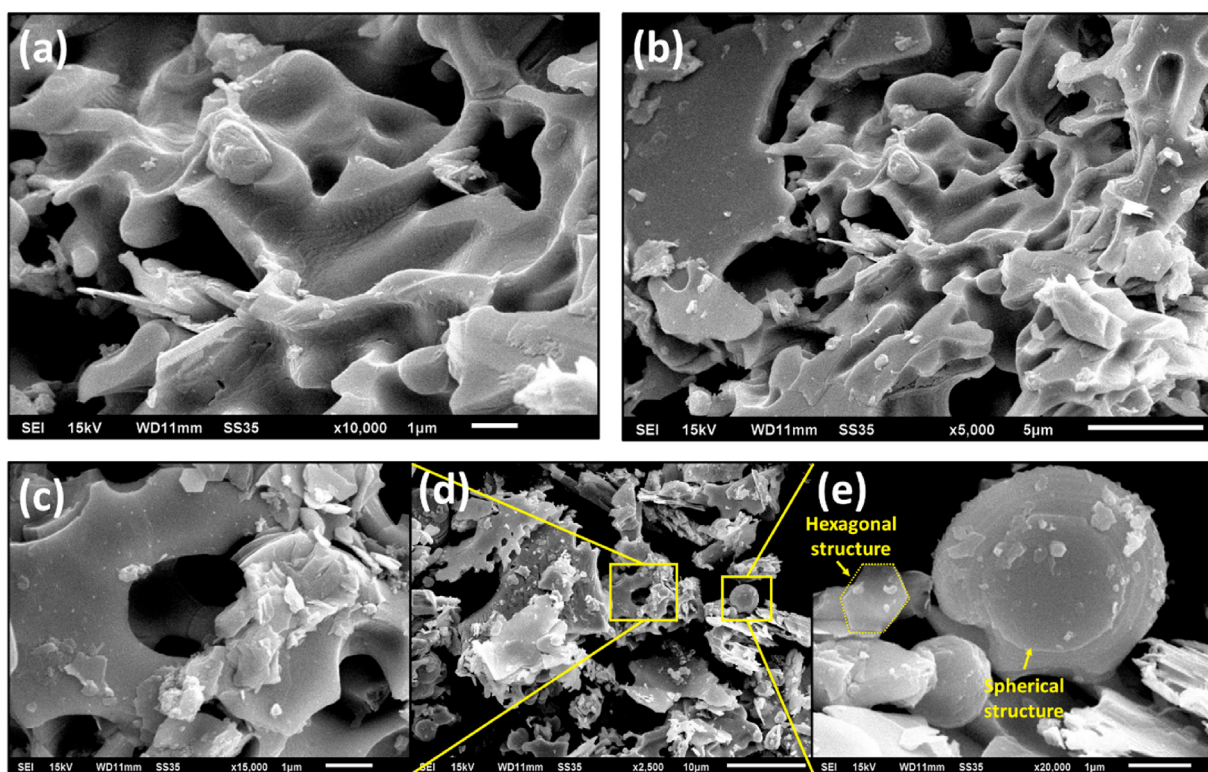


**Fig. 4.** SEM micrographs of the as-synthesized MoSe$_2$ powder.

layered structure of the MoSe$_2$ powder as expected (Fig. 6a and b). The spherical shaped microstructure was found to be made up of many layers that were also observed in SEM and FESEM measurements (Fig. 6c). These micrographs indicate the formation of layered nanosheets. The high-resolution TEM image of the sample is shown in Fig. 6d. The fringe width of 0.16 and 0.19 nm can be assigned to (110) and (105) planes of MoSe$_2$ powder. The plan view image of the sample shows the arrangement of atoms in a hexagonal lattice throughout the micrograph (Fig. 6e). The lattice constant calculated from this micrograph is 3.3 Å, which matches well with the lattice constant of 2H−MoSe$_2$. The extracted interlayer separation of 6.7 Å also agrees well with the previously reported XRD data [43]. The diffraction rings obtained in the selected area diffraction (SEAD) pattern of the sample are also consistent with the interplanar spacing of (002) and (116) planes of MoSe$_2$ (Fig. 6f).

### 3.5. Raman and BET

To further study the structure of the as-synthesized MoSe$_2$ powder, Raman spectroscopy was employed on the sample. The Raman spectrum of the as-prepared MoSe$_2$ nanosheets is shown in Fig. 7a. The B$_{2g}$ mode of MoO$_3$ and in-plane E$^1_{2g}$ mode of MoSe$_2$ were observed at ~197.6 and ~263.8 cm$^{-1}$ respectively [44,45]. The presence of MoO$_3$ in the Raman spectrum might be due to the surface oxidation of the sample when exposed to air. Further, the existence of the E$^1_{2g}$ mode of MoSe$_2$ confirms the formation of the 2H−MoSe$_2$ phase, which was found in the XRD analysis. The Nitrogen (N$_2$) adsorption-desorption isotherms and pore size distribution curves are shown in Fig. 7b. The BET measurements revealed that the mesoporous MoSe$_2$ structure exhibited a porosity of 0.17 cm$^3$ g$^{-1}$ and a specific surface area of 4.603 m$^2$ g$^{-1}$. In addition,
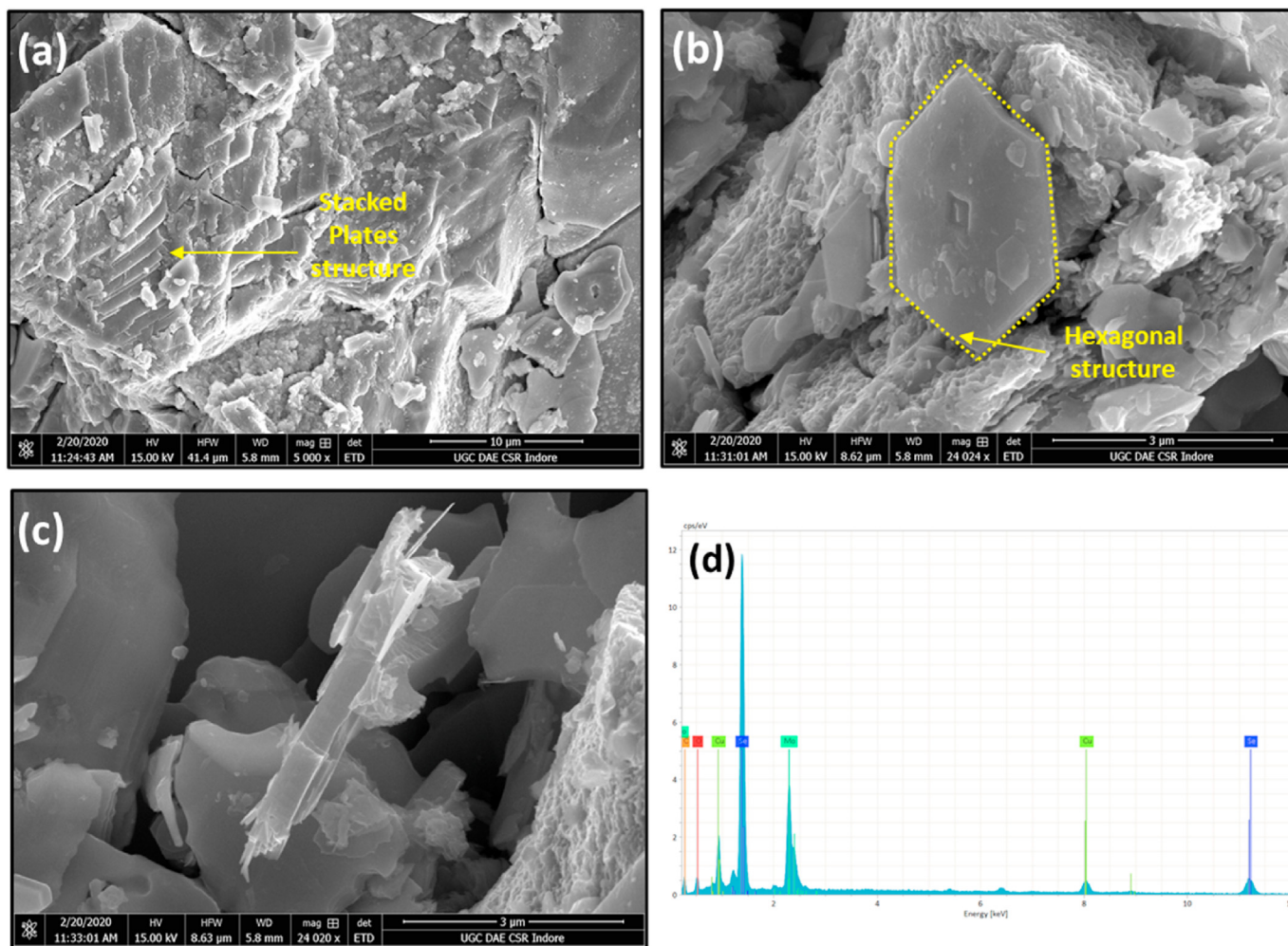
6

**Fig. 5.** (a), (b), (c) FESEM micrographs and (d) EDS of the as-prepared MoSe$_2$ powder.

**Table 2**
Element weight percent and atomic percent by EDS measurements of MoSe$_2$.

| S. No. | Element | Weight (%) | Atomic (%) |
|--------|---------|-----------|-----------|
| 1 | Mo | 36.76 | 32.36 |
| 2 | Se | 63.24 | 67.64 |

the average pore size has been calculated to be equal to about 2.479 nm. The pore size distribution is narrow (2−4 nm) which indicates the presence of a large number of micropores than mesopores. Such large specific surface area helps in the fast transportation of solvent into the nanopores and hence a high specific capacity can be achieved.

### 3.6. Electrochemical studies

The synthesized MoSe$_2$ powder was coated on a Ni foam and was used as a working electrode in a three-electrode system in 2 M KOH electrolyte solution which is generally used in supercapacitor measurements. Cyclic voltammetry (CV), galvanic charge-discharge (GCD), and electrochemical impedance spectroscopy (EIS) measurements were performed to estimate the electrochemical behavior of the MoSe$_2$ nanosheets (Fig. 8). Fig. 8a shows the CV curves of the MoSe$_2$ powder at different scan rates ranging from 5 to 125 mVs$^{-1}$ in the potential range of 0−0.4 V. Obviously, the CV curves of the MoSe$_2$ electrode are different from the ideal rectangular-shaped curves emerging from the electric double-layer capacitance. The redox peaks in the CV curves indicate the typical characteristic of Faraday behavior of the battery-like electrode (Fig. 8a). The set of redox peaks indicate that the specific capacitance (specific capacity) of the MoSe$_2$ nanosheets is mainly attributed to the faradic redox reactions between various valance states (i.e. conversion of Mo$^{4+}$ to Mo$^{3+}$ and vice versa) [13,46,47]. The cathodic peaks between 0.27 and 0.32 V can be attributed to the insertion of K$^+$ ions into the interlayers of MoSe$_2$ while the anodic peaks between 0.18 and 0.21 V correspond to the extraction of K$^+$ ions from the interlayers of MoSe$_2$. Therefore, the hexagonal MoSe$_2$ provides a diffusion path for the intercalation of K$^+$ and OH$^-$ ions. It can be observed that the reduction and oxidation peaks shift towards lower and higher voltages respectively with increasing scan rates. However, the shape of the curves is unvaried except for the small displacement in the peak positions. These results indicate that the electrode material possesses a low polarization effect and high electrochemical reversibility [48,49]. It should be noted that the contribution of Ni-foam to the specific capacitance can be ignored [50,51]. According to previous reports, the high value of specific capacitance may be accompanied by the combination of non-faradic (equation (11)) and faradic (equation (12)) processes of the MoSe$_2$ nanosheets [22,52].
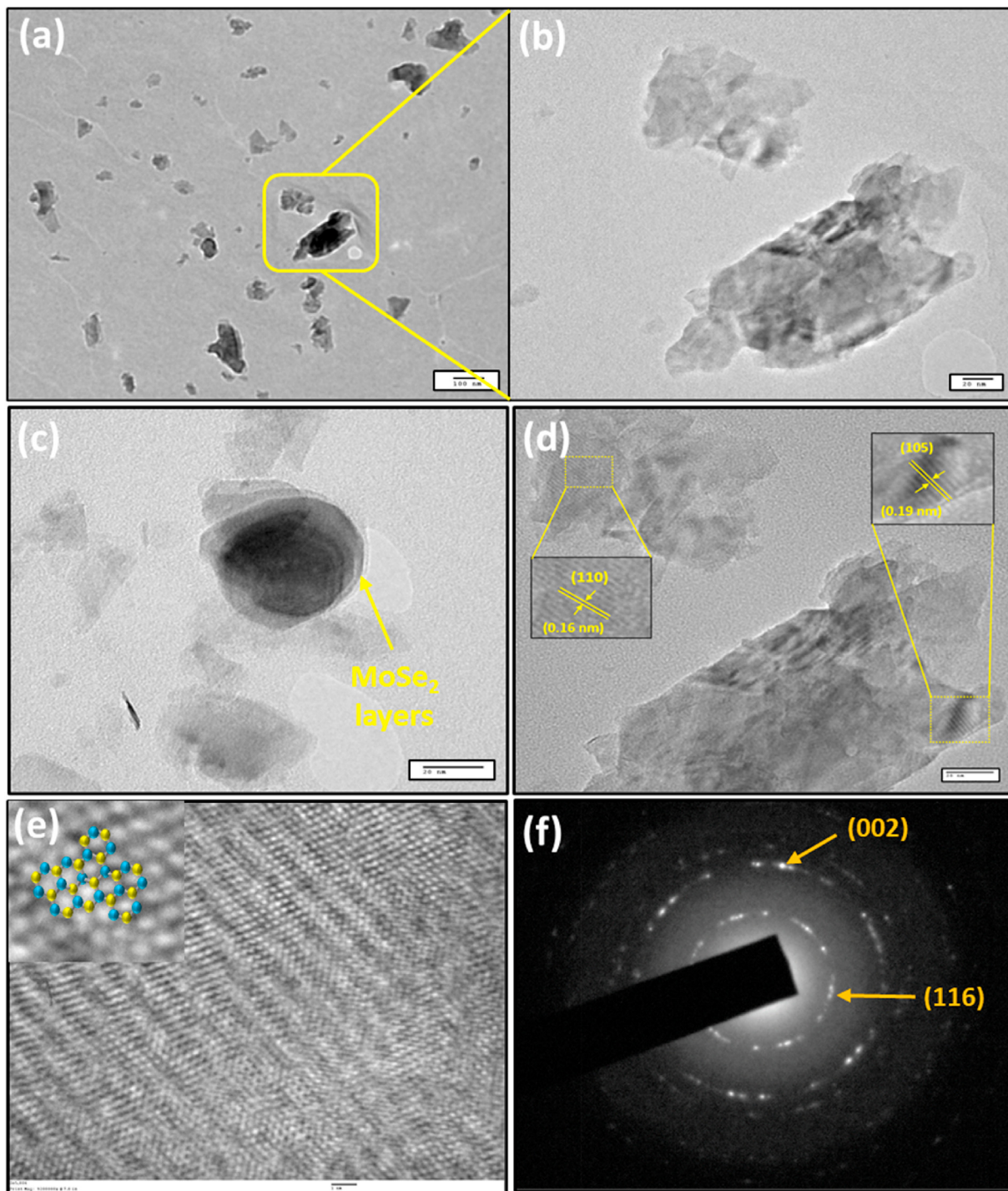
**Fig. 6.** (a), (b), (c) TEM micrographs, (d) high resolution TEM image, (e) Plan-view TEM image and (f) SEAD pattern of the $MoSe_2$ powder.

$$(MoSe_2)_{surface} + K^+ + e^- \leftrightarrow (MoSe_2-K)_{surface} \quad (11)$$

$$MoSe_2 + K^+ + e^- \leftrightarrow K-MoSe_2 \quad (12)$$

As shown in Fig. 8f, the linear behavior of the curve between the square root of the scan rate and peak current ($I_p$) of anodic and cathodic sweep indicates the excellent reversibility of the $MoSe_2$ electrode. Also, it indicates that the reaction is mainly controlled by the diffusion of $OH^-$ ions and confirms the Faradic redox behavior of the charge-storage rather than EDL adsorption [53]. The

capacitance contribution of the electrode material can be described from the CV curves using the power low as given below [54].

$$I = av^b \quad (13)$$

Here "I" is the anodic current (mA), "v" is the scan rate and "a" and "b" are the adjustable parameters. The b value can be determined from the slope of the log I versus log v as shown in Fig. 8g. It is well defined that, If the value of b is equal to 0.5, the charge storage mechanism will be diffusion-limited. And if b is equal to 1,
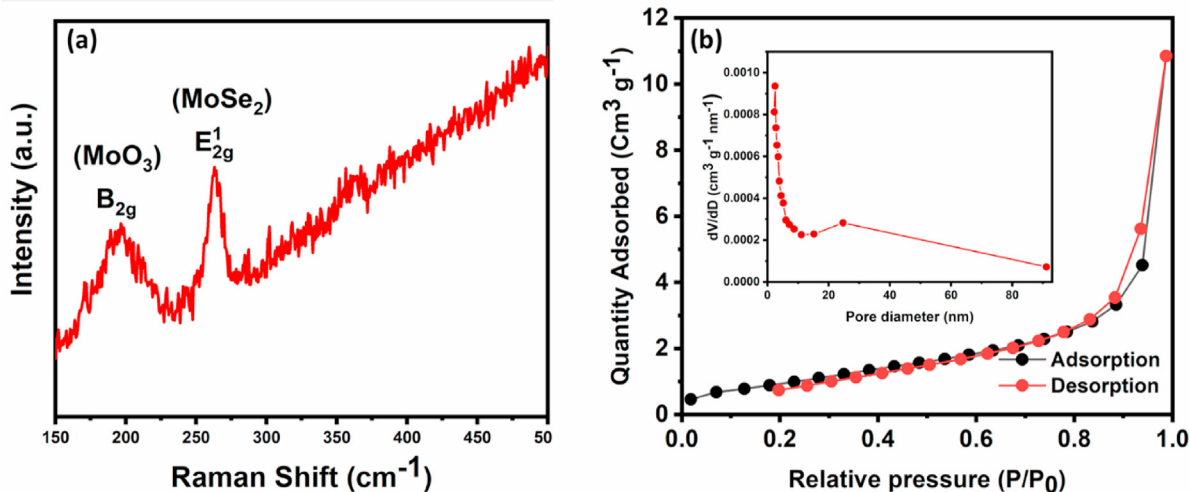
S. Upadhyay and O.P. Pandey

**Fig. 7.** (a) Raman spectra and (b) $N_2$ adsorption-desorption isotherms and pore size distribution curve of as-prepared $MoSe_2$ powder.

the charge storage mechanism will be capacitive. The value of b for the prepared $MoSe_2$ has been calculated to be equal to 0.73. It indicates that the overall capacitance is a combination of surface and diffusion capacitive processes. A quantitative contribution of surface capacitive and diffusion on the overall specific capacitance can be determined using the following expression [55].

$$I(V) = k_1 v + k_2 v^{1/2} \tag{14}$$

$$I(V) \Big/ v^{1/2} = k_1 v^{1/2} + k_2 \tag{15}$$

Here $k_1 v$ is the contribution from the surface capacitive part and $k_2 v^{1/2}$ correspond to the contribution from the diffusion-limited to the overall specific capacitance. The values of $k_1$ and $k_2$ can be determined from the slope and intercept of the curve between $I_p/v^{1/2}$ and $v^{1/2}$ (Fig. 8h). Therefore, the value of $k_1$ and $k_2$ has been calculated from Fig. 8h. The current contributions of the surface capacitive and diffusion-limited to overall specific capacity at different scan rates are shown in Fig. 8i. It can be observed that the surface capacitive contribution increases with increasing scan rates. The surface capacitive contribution was 26.2% at 5 mV s$^{-1}$ which increased to 63.9% at 125 mV s$^{-1}$.

The electrochemical behavior of the $MoSe_2$ powder was further investigated using Galvanic charge-discharge (GCD) measurements. GCD allows us to calculate the specific capacity of ECs at a constant current. Fig. 8b displays the GCD curves of the $MoSe_2$ nanosheets at various current densities. The specific capacity (specific capacitance) values were calculated to be equal to 46.22 mAh g$^{-1}$ (115 Fg$^{-1}$), 41.88 mAh g$^{-1}$ (104.7 Fg$^{-1}$), 38.32 mAh g$^{-1}$ (95.8 Fg$^{-1}$), 35.5 mAh g$^{-1}$ (88.75 Fg$^{-1}$), 31.2 mAh g$^{-1}$ (78 Fg$^{-1}$), and 30 mAh g$^{-1}$ (75 Fg$^{-1}$) at a current density of 2, 3, 4, 5, 8, and 10 Ag$^{-1}$ respectively. The detailed calculation steps of specific capacity have been discussed in the experimental section. Fig. 8c shows the relationship between the specific capacity of the $MoSe_2$ nanosheets and various current densities. The value of specific capacity decreases when the current density increases and a sudden drop can be observed from 2 Ag$^{-1}$ to 4 Ag$^{-1}$ and thereafter, it decreases gradually. These results are consistent with the CV data. Also, similar to the CV analysis, the diffusion rate of the electrons and ions in the electrolyte is limited and hence only the surface area of the $MoSe_2$ nanosheets takes part in the electrochemical process at higher current densities. However, the electrolyte ions could

penetrate the outer surface of the $MoSe_2$ nanosheets at lower current densities, and hence the interior part of the electrode material is reachable and responsible for the higher value of the specific capacity. Table S1 shows the comparison of the electrochemical performance of the prepared $MoSe_2$ powder with other reported $MoSe_2$ electrodes.

An endurance test was done to investigate the stability of the electrode material via galvanic charge-discharge measurements at a current density of 5 Ag$^{-1}$ up to 2000 cycles. The graph between specific capacity and the number of cycles is shown in Fig. 8d. A dramatic decrement in the specific capacity of the $MoSe_2$ nanosheets (25%) has been observed after 1000 cycles. Therefore, it can be concluded that the prepared $MoSe_2$ powder exhibited low cyclic stability. This capacity loss perhaps originating from the saturation of active sites of the $MoSe_2$ surface during the charging-discharging process [56]. Thereafter a gradual decrease in the specific capacity of the electrode was observed up to 2000 GCD cycles. It has been observed that the $MoSe_2$ nanosheets retain the specific capacity at 56.5 mAh g$^{-1}$ (about 64% of the initial capacity) over 2000 cycles. It showed a poor coulombic efficiency of 88% after the first cycle, which is better than some of the previously reported literature [52,57]. Further, it increases to 90% even after 2000 cycles at a current density of 5 A g$^{-1}$. Such poor coulombic efficiency of the $MoSe_2$ electrode might be due to the interactions between electrode or electrolyte with impurities and the parasitic (ageing) chemical reactions that occur between the electrode/electrolyte interface. The chemical instability of the $MoSe_2$ nanosheets in the aqueous electrolyte might be responsible for the capacity loss of 36%, which can be improved by using non-aqueous electrolytes based on organic liquids.

EIS measurements at different overpotentials were conducted to confirm the battery-like behavior of the electrode material. It also helps us to understand the charge transfer kinetics of the supercapacitor electrode material. Fig. 8e shows the Nyquist plots obtained from the EIS measurements of the $MoSe_2$ nanosheets at various potentials. An equivalent electrical circuit was developed to get the information from the Nyquist plots based on the experimental data as shown in Fig. 8e. The first element ($R_1 = R_s$) of the circuit represents the resistance imposed by the electrical circuit and electrolyte [58]. It was observed that there is no significant change in the electric resistance $R_s$ at different bias voltages ($R_s$ 0.85$\Omega$). As shown in Fig. 8e, the impedance spectrums depicting

*S. Upadhyay and O.P. Pandey*
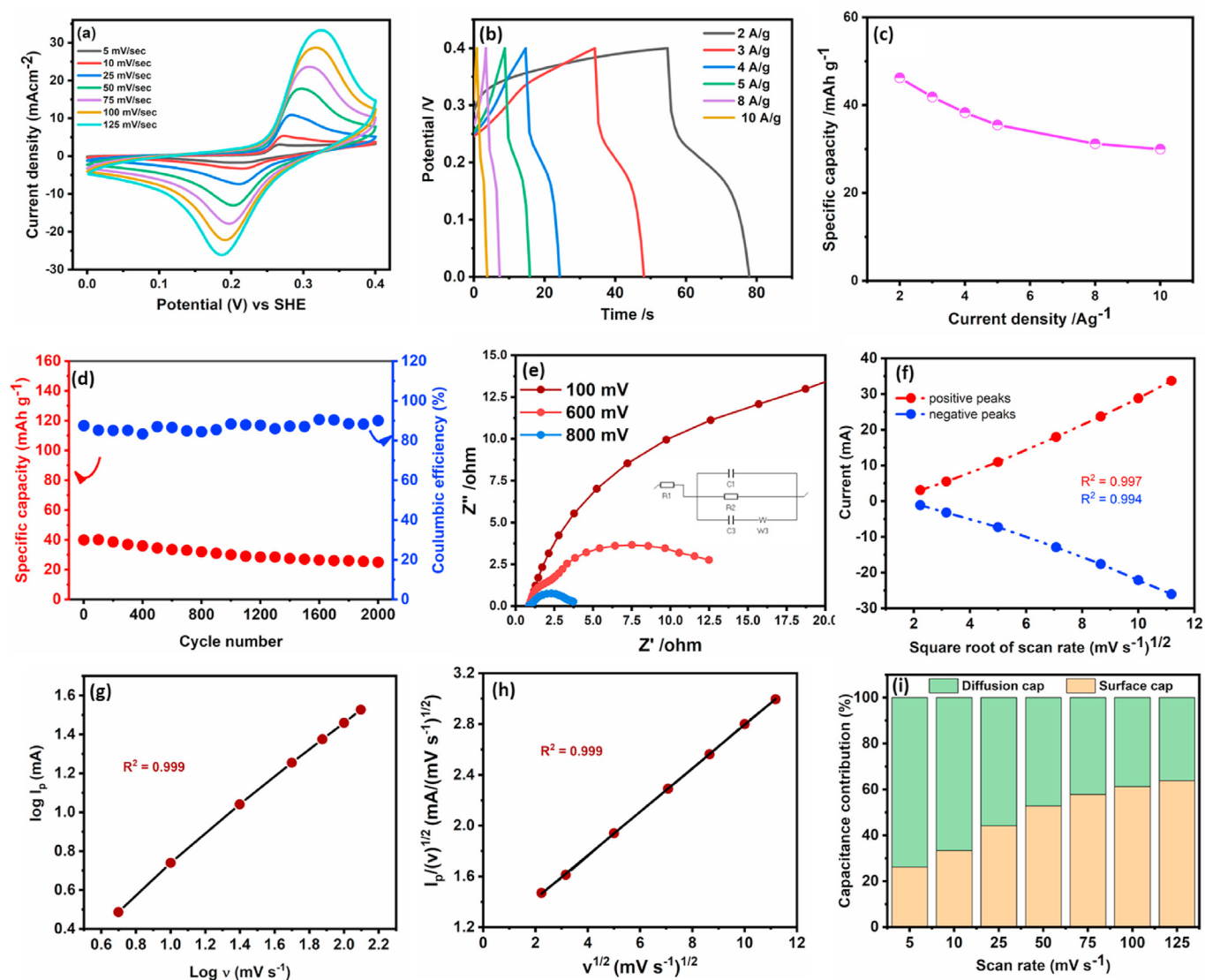
**Fig. 8.** (a) CV curves at different scan rates, (b) GCD curves at different current densities, (c) current density versus specific capacitance estimated from GCD curves, (d) cyclic stability and coulombic efficiency at a current density of 5 A/g and (e) EIS curves at different overpotentials, (f) graph between current versus square root of scan rate, (g) Plot of log $(I_p)$ vs log $(v)$ (anodic sweep), (h) Plot of $(I_p/v^{1/2})$ against the square root of scan rate $(v^{1/2})$, (i) variation of specific capacitance as a function of scan rate showing the capacitive and diffusion-limited contribution to the total capacitance of MoSe$_2$ nanosheets.

semicircles at higher frequencies are mainly attributed to the interfacial charge transfer resistance ($R_2 = R_{ct}$) of the ions in the electrode-electrolyte interface caused by faraday reaction [59]. In Fig. 8e, it can be observed that with increasing bias voltage, the diameter of the semicircle decreases which indicates the strong dependence on bias voltage, and reaction kinetics. The value of $R_{ct}$ was calculated to be equal to 71.71, 12.6, and 6.5 $\Omega$ at 100, 600, and 800 mV respectively. The nearly linear behavior of the charge transfer resistance with increasing overpotential can be attributed to the high surface area and uniform porous structure (Fig. S4; SI). Also, the linear decrement in the $R_{ct}$ value confirms the pseudo-capacitive or battery-like behavior of the prepared MoSe$_2$ powder. The electron transfer reaction is limited at low overpotential however, at high overpotentials the rate of electron transfer increases, and charge transfer resistance decreases [60]. Therefore, the difference is attributed to the favored charge transport processes within the porous structure of the MoSe$_2$ electrode.

Further to investigate the feasibility of the as-synthesized MoSe$_2$

nanosheets for practical applications, an asymmetric super-capacitor has been fabricated using MoSe$_2$ electrodes as anode and cathode materials both. The electrochemical measurements of the MoSe$_2$ SSC are shown in Fig. 9. Whatman paper/KOH has been used as a solid electrolyte and the digital photograph of the as-fabricated MoSe$_2$ SSC is shown in Fig. 9a. Initially, CV and GCD curves at different potential windows (0–0.5 V, 0–0.6 V, 0–0.7 V, 0–0.8 V, and 0–0.9 V) were measured and are shown in Fig. 9b and c, respectively. The CV curves were measured at a scan rate of 100 mV s$^{-1}$ while the GCD curves were measured at a current density of 1 Ag$^{-1}$. From these curves, it can be concluded that the MoSe$_2$ SSC can operate at a potential window of 0–0.6 V as the rectangular shape of the CV curves is highly distorted above 0.6 V.

The CV curves at various scan rates ranging from 10 to 90 mV s$^{-1}$ within a voltage window of 0–0.6 V are shown in Fig. 9d. The shape of the CV curves has not changed significantly with a gradual increase in the scan rate from 10 to 90 mV s$^{-1}$, indicating the outstanding capacitive property of the MoSe$_2$ SSC [61]. However,
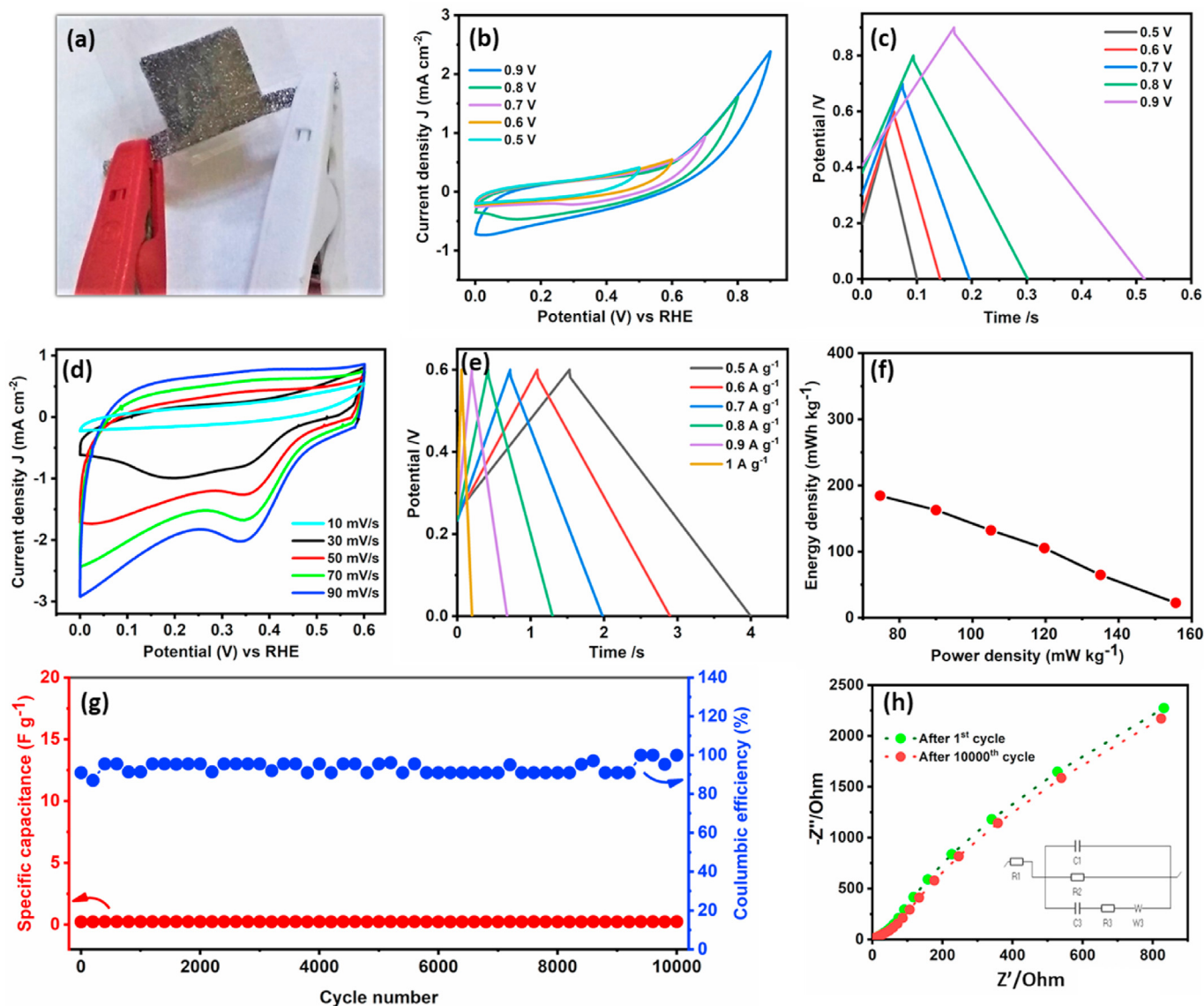
**Fig. 9.** Electrochemical performance of as-assembled $MoSe_2$ SSC device. (a) digital photograph of $MoSe_2$ SSC, (b) CV and (c) GCD curves at various potential windows, (d) CV curves at different scan rates, (e) GCD curves at various current densities, (f) Ragone plot, (g) cyclic performance and coulombic efficiency at 1 A $g^{-1}$ and (h) EIS curves before and after 10000 cycles.

the presence of redox peaks around 0.3−0.4 V at higher scan rates demonstrating the pseudocapacitive behavior of the $MoSe_2$ SSC. Also, the GCD curves at different current densities ranging from 0.5 to 1 A$g^{-1}$ are shown in Fig. 9e. These curves showed almost symmetrical behavior in the overall range of the current densities measured, which indicates high reversibility of the SSC [62,63]. The specific capacitance has been calculated to be equal to 4.1, 3.62, 2.94, 2.34, 1.44, 0.5 F$g^{-1}$ at a current density of 0.5, 0.6, 0.7, 0.8, 0.9, 1 A $g^{-1}$ respectively. The Ragone plot, which shows the relationship between power and current density of the $MoSe_2$ SSC is shown in Fig. 9f. It was found that the high energy density of 184.5 mWh kg$^{-1}$ can be achieved at a power density of 74.6 mW kg$^{-1}$ at a constant current density of 0.5 A g$^{-1}$. Also, it can maintain an energy density of 22.6 mWh kg$^{-1}$ at a high-power density of 155.6 mW kg$^{-1}$ indicating a good rate capability of the $MoSe_2$ SSC.

Fig. 9g shows the cyclic stability and coulombic efficiency curves of the $MoSe_2$ SSC at a constant current density of 1 A g$^{-1}$ for 10000 GCD cycles. Eventually, the device delivered high cyclic stability

with capacitance retention of 105% of the initial capacitance even after 10000 GCD cycles. Also, it shows a high coulombic efficiency of nearly 98% after the first cycle while it increases to 100% after 10000 cycles. The electrochemical impedance spectroscopy (EIS) has been conducted to understand the fundamental behavior of the as-fabricated $MoSe_2$ SSC. Fig. 9h shows the Nyquist plots for the $MoSe_2$ SSC over the frequency range of $10^2-10^{-2}$ kH$_z$ before and after 10000 cycles. The x-intercept at the beginning of the Z'-axis represents the equivalent resistance of the contact and electrolyte resistance (ESR). The ESR value of $MoSe_2$ before cycling is 0.389 Ω however, after 10000 cycles it charges to 0.439 Ω. The small change of about 0.05 Ω in the ESR indicating the structural stability of the electrode material. On the other hand, the charge transfer resistance ($R_{ct}$) decreases from 9 Ω to 8.2 Ω before and after 10000 cycles respectively, which indicates the high charge transport of electrolyte ions. These results confirm the high suitability of the as-synthesized $MoSe_2$ material for supercapacitor applications.

## 4. Conclusion

In summary, layered MoSe$_2$ nanosheets have been successfully prepared by a simple in-situ selenization route and studied their electrochemical capacitance properties in 2 M KOH electrolyte. The synthesis mechanism and the influence of the reaction parameters on the phase formation have been studied. The SEM and FESEM results reveal that the MoSe$_2$ nanosheets are made up of porous network and stacked plate structures. Further, TEM and Raman measurements confirm the formation of layered 2H−MoSe$_2$ nanosheets, which was found in the XRD analysis. The MoSe$_2$ nanosheets as an electrode material exhibited a high specific capacity of 46.22 mAh g$^{-1}$ at a current density of 2 Ag$^{-1}$. The high specific capacity of the electrode is mainly due to the layered structure of the MoSe$_2$ nanosheets along with the porous network, which provides a high specific surface area and fast electrolyte ion transport. Also, the MoSe$_2$ nanosheets maintain the specific capacity to 64% of the primary value after 2000 cycles. In addition, the assembled MoSe$_2$ SSC device delivered a good specific capacitance of 4.1 Fg$^{-1}$ at a current density of 0.5 A g$^{-1}$. It exhibited high cyclic stability with capacitance retention of 105% of the initial capacitance and a high coulombic efficiency of 100% even after 10000 cycles. The high specific capacitance and long cycle life suggest that the prepared MoSe$_2$ nanosheets could be a potential candidate for high-performance electrochemical supercapacitor.

## CRediT authorship contribution statement

**Sanjay Upadhyay:** Conceptualization, Methodology, Software, Investigation, Data curation, Writing - original draft, preparation, Visualization. **O.P. Pandey:** Supervision, Writing - review & editing.

## Declaration of competing interest

The authors declare that they have no known competing financial interests or personal relationships that could have appeared to influence the work reported in this paper.

## Acknowledgment

## Appendix A. Supplementary data

Supplementary data related to this article can be found at https://doi.org/10.1016/j.jallcom.2020.157522.

## References

[1] C. Yu, P. Ma, X. Zhou, A. Wang, T. Qian, S. Wu, Q. Chen, All-solid-state flexible supercapacitors based on highly dispersed polypyrrole nanowire and reduced graphene oxide composites, ACS Appl. Mater. Interfaces 6 (2014) 17937−17943, https://doi.org/10.1021/am5059603.

[2] A. Ramadoss, B. Saravanakumar, S.W. Lee, Y.S. Kim, S.J. Kim, Z.L. Wang, Piezoelectric-driven self-charging supercapacitor power cell, ACS Nano 9 (2015) 4337−4345, https://doi.org/10.1021/acsnano.5b00759.

[3] V. Veeramani, R. Madhu, S.M. Chen, M. Sivakumar, Flower-like nickel-cobalt oxide decorated dopamine-derived carbon nanocomposite for high performance supercapacitor applications, ACS Sustain. Chem. Eng. 4 (2016) 5013−5020, https://doi.org/10.1021/acssuschemeng.6b01391.

[4] J. Yan, Q. Wang, T. Wei, Z. Fan, Recent advances in design and fabrication of electrochemical supercapacitors with high energy densities, Adv. Energy Mater. 4 (2014) 1300816, https://doi.org/10.1002/aenm.201300816.

[5] H. Ji, X. Zhao, Z. Qiao, J. Jung, Y. Zhu, Y. Lu, L.L. Zhang, A.H. MacDonald, R.S. Ruoff, Capacitance of carbon-based electrical double-layer capacitors, Nat. Commun. 5 (2014) 1−7, https://doi.org/10.1038/ncomms4317.

[6] Y. Liu, B. Soucaze-Guillous, P.L. Taberna, P. Simon, Understanding of carbon-based supercapacitors ageing mechanisms by electrochemical and analytical methods, J. Power Sources 366 (2017) 123−130, https://doi.org/10.1016/j.jpowsour.2017.08.104.

[7] E. Frackowiak, Carbon materials for supercapacitor application, Phys. Chem. Chem. Phys. 9 (2007) 1774−1785, https://doi.org/10.1039/b618139m.

[8] N. Zhao, S. Wu, C. He, C. Shi, E. Liu, X. Du, J. Li, Hierarchical porous carbon with graphitic structure synthesized by a water soluble template method, Mater. Lett. 87 (2012) 77−79, https://doi.org/10.1016/j.matlet.2012.07.085.

[9] S.M. Djuric, G. Kitic, G. Dubourg, R. Gajic, T. Tomasevic-Ilic, V. Minic, M. Spasenovic, Miniature graphene-based supercapacitors fabricated by laser ablation, Microelectron. Eng. 182 (2017) 1−7, https://doi.org/10.1016/j.mee.2017.08.005.

[10] H.J. Kim, S.Y. Lee, L.H. Sinh, C.S. Yeo, Y.R. Son, K.R. Cho, Y.K. Song, S. Ju, M.K. Shin, S.J. Park, S.Y. Park, Maximizing volumetric energy density of all-graphene-oxide-supercapacitors and their potential applications for energy harvest, J. Power Sources 346 (2017) 113−119, https://doi.org/10.1016/j.jpowsour.2017.02.040.

[11] Y. Liu, X. Peng, Recent advances of supercapacitors based on two-dimensional materials, Appl. Mater. Today. 8 (2017) 104−115, https://doi.org/10.1016/j.apmt.2017.05.002.

[12] M. Buscema, J.O. Island, D.J. Groenendijk, S.I. Blanter, G.A. Steele, H.S.J. Van Der Zant, A. Castellanos-Gomez, Photocurrent generation with two-dimensional van der Waals semiconductors, Chem. Soc. Rev. 44 (2015) 3691−3718, https://doi.org/10.1039/c5cs00106d.

[13] F. Paquin, J. Rivnay, A. Salleo, N. Stingelin, C. Silva, Multi-phase semicrystalline microstructures drive exciton dissociation in neat plastic semiconductors, J. Mater. Chem. C. 3 (2015) 10715−10722, https://doi.org/10.1039/b000000x.

[14] H. Wang, H. Feng, J. Li, Graphene and graphene-like layered transition metal dichalcogenides in energy conversion and storage, Small 10 (2014) 2165−2181, https://doi.org/10.1002/smll.201303711.

[15] C.N.R. Rao, U. Maitra, U.V. Waghmare, Extraordinary attributes of 2-dimensional MoS$_2$ nanosheets, Chem. Phys. Lett. 609 (2014) 172−183, https://doi.org/10.1016/j.cplett.2014.06.003.

[16] W. Choi, M.Y. Cho, A. Konar, J.H. Lee, G.B. Cha, S.C. Hong, S. Kim, J. Kim, D. Jena, J. Joo, S. Kim, High-detectivity multilayer MoS$_2$ phototransistors with spectral response from ultraviolet to infrared, Adv. Mater. 24 (2012) 5832−5836, https://doi.org/10.1002/adma.201201909.

[17] H. Li, K. Yu, X. Lei, B. Guo, C. Li, H. Fu, Z. Zhu, Synthesis of the MoS$_2$@CuO heterogeneous structure with improved photocatalysis performance and H2O adsorption analysis, Dalton Trans. 44 (2015) 10438−10447, https://doi.org/10.1039/c5dt01125f.

[18] M. Pumera, Z. Sofer, A. Ambrosi, Layered transition metal dichalcogenides for electrochemical energy generation and storage, J. Mater. Chem. A. 2 (2014) 8981−8987, https://doi.org/10.1039/c4ta00652f.

[19] J.M. Soon, K.P. Loh, Electrochemical double-layer capacitance of MoS$_2$ nanowall films, Electrochem. Solid State Lett. 10 (2007) 250−254, https://doi.org/10.1149/1.2778851.

[20] X. Hu, W. Zhang, X. Liu, Y. Mei, Y. Huang, Nanostructured Mo-based electrode materials for electrochemical energy storage, Chem. Soc. Rev. 44 (2015) 2376−2404, https://doi.org/10.1039/c4cs00350k.

[21] H. Li, L. Chen, Y. Zhang, X. Ji, S. Chen, H. Song, C. Li, H. Tang, Synthesis of MoSe$_2$/Reduced graphene oxide composites with improved tribological properties for oil-based additives, Cryst. Res. Technol. 49 (2014) 204−211, https://doi.org/10.1002/crat.201300317.

[22] S.K. Balasingam, J.S. Lee, Y. Jun, Few-layered MoSe$_2$ nanosheets as an advanced electrode material for supercapacitors, Dalton Trans. 44 (2015) 15491−15498, https://doi.org/10.1039/c5dt01985k.

[23] Y.P. Gao, K.J. Huang, H.L. Shuai, L. Liu, Synthesis of sphere-feature molybdenum selenide with enhanced electrochemical performance for supercapacitor, Mater. Lett. 209 (2017) 319−322, https://doi.org/10.1016/j.matlet.2017.08.044.

[24] Z. Zhang, X. Yang, Y. Fu, K. Du, Ultrathin molybdenum diselenide nanosheets anchored on multi-walled carbon nanotubes as anode composites for high performance sodium-ion batteries, J. Power Sources 296 (2015) 2−9, https://doi.org/10.1016/j.jpowsour.2015.07.008.

[25] Y. Qiu, X. Li, M. Bai, H. Wang, D. Xue, W. Wang, J. Cheng, Flexible full-solid-state supercapacitors based on self-assembly of mesoporous MoSe$_2$ nanomaterials, Inorg. Chem. Front. 4 (2017) 675−682, https://doi.org/10.1039/c6qi00569a.

[26] J.S.L., Y.J. Suresh Kannan Balasingam, Molybdenum diselenide/reduced graphene oxide based hybrid nanosheets for supercapacitor applications, Dalton Trans. 45 (2016) 9646−9653, https://doi.org/10.1039/C6DT00449K.

S. Upadhyay and O.P. Pandey

[27] P. Pazhamalai, K. Krishnamoorthy, S. Sahoo, S. Kim, Two-dimensional molybdenum diselenide nanosheets as a novel electrode material for symmetric supercapacitors using organic electrolyte, Electrochim. Acta 295 (2019) 591–598, https://doi.org/10.1016/j.electacta.2018.10.191.

[28] C. Li, Y. Zhou, P. Huo, X. Wang, Fabricated high performance ultrathin $MoSe_2$ nanosheets grow on MWCNT hybrid materials for asymmetric supercapacitors, J. Alloys Compd. 826 (2020) 154175, https://doi.org/10.1016/j.jallcom.2020.154175.

[29] C. He, J. Tao, Two-dimensional TaC nanosheets on a reduced graphene oxide hybrid as an efficient and stable electrocatalyst for water splitting, Chem. Commun. 52 (2016) 8810–8813, https://doi.org/10.1039/c6cc03876j.

[30] I.V. Mishakov, A.F. Bedilo, R.M. Richards, V.V. Chesnokov, A.M. Volodin, V.I. Zaikovskii, R.A. Buyanov, K.J. Klabunde, Nanocrystalline MGO as a dehydrohalogenation catalyst, J. Catal. 206 (2002) 40–48, https://doi.org/10.1006/jcat.2001.3474.

[31] S.H. Wanamaker, K.J. Schmitt, D.A. Lupher, N.C. Stockman, D.S. Brooks, R.A. Parks, T.D. Reist, M.R. Kyle, P.L. Muio, Designing A reactor to generate hydrogen bubbles, Chem. Educ. 5 (2000) 14–16, https://doi.org/10.1007/s00897990351a.

[32] K. Yoshida, Y. Takahashi, R. Ihara, N. Terakado, T. Fujiwara, H. Kato, M. Kakihana, Large enhancement of photocatalytic activity by chemical etching of $TiO_2$ crystallized glass, Apl. Mater. 2 (2014) 106103, https://doi.org/10.1063/1.4897961.

[33] M. Wu, B. Wang, Q. Hu, L. Wang, A. Zhou, The synthesis process and thermal stability of $V_2C$ MXene, Materials 11 (2018) 2112, https://doi.org/10.3390/ma11112112.

[34] L.K. Brar, G. Singla, O.P. Pandey, Evolution of structural and thermal properties of carbon-coated TaC nanopowder synthesized by single step reduction of Ta-ethoxide, RSC Adv. 5 (2015) 1406–1416, https://doi.org/10.1039/c4ra12105h.

[35] K. Inzani, M. Nematollahi, S.M. Selbach, T. Grande, F. Vullum-Bruer, Progression of reduction of $MoO_3$ observed in powders and solution-processed films, Thin Solid Films 626 (2017) 94–103, https://doi.org/10.1016/j.tsf.2017.02.029.

[36] S.V. Aydinyan, Z. Gumruyan, K.V. Manukyan, S.L. Kharatyan, Self-sustaining reduction of $MoO_3$ by the Mg-C mixture, Mater. Sci. Eng. B Solid-State Mater. Adv. Technol. 172 (2010) 267–271, https://doi.org/10.1016/j.mseb.2010.05.028.

[37] Q. Hao, G. Cui, Y. Zhao, Z. Bakenov, Flower-like $MoSe_2/MoO_2$ composite with high capacity and long-term stability for lithium-ion battery, Nanomaterials 9 (2019) 1256, https://doi.org/10.3390/nano9091256.

[38] Y. Huang, Y.E. Miao, J. Fu, S. Mo, C. Wei, T. Liu, Perpendicularly oriented few-layer $MoSe_2$ on $SnO_2$ nanotubes for efficient hydrogen evolution reaction, J. Mater. Chem. A. 3 (2015) 16263–16271, https://doi.org/10.1039/c5ta03704b.

[39] R.A. Mir, O.P. Pandey, Waste plastic derived carbon supported $Mo_2C$ composite catalysts for hydrogen production and energy storage applications, J. Clean. Prod. 218 (2019) 644–655, https://doi.org/10.1016/j.jclepro.2019.02.004.

[40] P. Ge, H. Hou, C.E. Banks, C.W. Foster, S. Li, Y. Zhang, J. He, C. Zhang, X. Ji, Binding $MoSe_2$ with carbon constrained in carbonous nanosphere towards high-capacity and ultrafast Li/Na-ion storage, Energy Storage Mater 12 (2018) 310–323, https://doi.org/10.1016/j.ensm.2018.02.012.

[41] R. Sadri, M. Hosseini, S.N. Kazi, S. Bagheri, N. Zubir, K.H. Solangi, T. Zaharinie, A. Badarudin, A bio-based, facile approach for the preparation of covalently functionalized carbon nanotubes aqueous suspensions and their potential as heat transfer fluids, J. Colloid Interface Sci. 504 (2017) 115–123, https://doi.org/10.1016/j.jcis.2017.03.051.

[42] D. Yang, A. Velamakanni, G. Bozoklu, S. Park, M. Stoller, R.D. Piner, S. Stankovich, I. Jung, D.A. Field, C.A. Ventrice, R.S. Ruoff, Chemical analysis of graphene oxide films after heat and chemical treatments by X-ray photo-electron and Micro-Raman spectroscopy, Carbon N. Y. 47 (2009) 145–152, https://doi.org/10.1016/j.carbon.2008.09.045.

[43] P.B. James, M.T. Lavik, The crystal structure of $MoSe_2$, Acta Crystallogr. 16 (1963) 1183, https://doi.org/10.1107/s0365110x6300311x, 1183.

[44] S.K.S. Patel, K. Dewangan, S.K. Srivastav, N.K. Verma, P. Jena, A.K. Singh, N.S. Gajbhiye, Synthesis of α-$MoO_3$ nanofibers for enhanced field-emission properties, Adv. Mater. Lett. 9 (2018) 585–589, https://doi.org/10.5185/amlett.2018.2022.

[45] C.T. Wu, S.Y. Hu, K.K. Tiong, Y.C. Lee, Anisotropic effects in the Raman scattering of Re-doped 2H-$MoSe_2$ layered semiconductors, Results Phys 7 (2017) 4096–4100, https://doi.org/10.1016/j.rinp.2017.10.033.

[46] J. Yang, C. Wang, H. Ju, Y. Sun, S. Xing, J. Zhu, Q. Yang, Integrated quasiplane heteronanostructures of $MoSe_2/Bi_2Se_3$ hexagonal nanosheets: synergetic electrocatalytic water splitting and enhanced supercapacitor performance, Adv. Funct. Mater. 27 (2017) 1–10, https://doi.org/10.1002/adfm.201703864.

[47] K.J. Huang, J.Z. Zhang, J.L. Cai, Preparation of porous layered molybdenum selenide-graphene composites on Ni foam for high-performance supercapacitor and electrochemical sensing, Electrochim. Acta 180 (2015) 770–777, https://doi.org/10.1016/j.electacta.2015.09.016.

[48] X. Chang, W. Li, Y. Liu, M. He, X. Zheng, X. Lv, Z. Ren, Synthesis and characterization of $NiCo_2O_4$ nanospheres/nitrogen-doped graphene composites with enhanced electrochemical performance, J. Alloys Compd. 784 (2019) 293–300, https://doi.org/10.1016/j.jallcom.2019.01.036.

[49] P. Yang, W. Mai, Flexible solid-state electrochemical supercapacitors, Nano-mater. Energy 8 (2014) 274–290, https://doi.org/10.1016/j.nanoen.2014.05.022.

[50] X. Mao, Z. Wang, W. Kong, W. Wang, Nickel foam supported hierarchical $Co_9S_8$ nanostructures for asymmetric supercapacitors, New J. Chem. 41 (2017) 1142–1148, https://doi.org/10.1039/c6nj02800d.

[51] X.Q. Zhang, W. Dong, A.H. Lu, W.C. Li, Rational design of mesoporous carbon electrodes with high mass loading for binder-free supercapacitors, Energy Technol. 3 (2015) 234–241, https://doi.org/10.1002/ente.201402161.

[52] S.S. Karade, B.R. Sankapal, Two dimensional cryptomelane like growth of $MoSe_2$ over MWCNTs: symmetric all-solid-state supercapacitor, J. Electroanal. Chem. 802 (2017) 131–138, https://doi.org/10.1016/j.jelechem.2017.08.017.

[53] L. Du, W. Du, H. Ren, N. Wang, Z. Yao, X. Shi, B. Zhang, J. Zai, X. Qian, Honeycomb-like metallic nickel selenide nanosheet arrays as binder-free electrodes for high-performance hybrid asymmetric supercapacitors, J. Mater. Chem. A. 5 (2017) 22527–22535, https://doi.org/10.1039/c7ta06921a.

[54] V. Augustyn, J. Come, M.A. Lowe, J.W. Kim, P.L. Taberna, S.H. Tolbert, H.D. Abruña, P. Simon, B. Dunn, High-rate electrochemical energy storage through $Li^+$ intercalation pseudocapacitance, Nat. Mater. 12 (2013) 518–522, https://doi.org/10.1038/nmat3601.

[55] J. Wang, J. Polleux, J. Lim, B. Dunn, Pseudocapacitive contributions to electrochemical energy storage in $TiO_2$ (anatase) nanoparticles, J. Phys. Chem. C 111 (2007) 14925–14931, https://doi.org/10.1021/jp074464w.

[56] L. Cao, S. Yang, W. Gao, Z. Liu, Y. Gong, L. Ma, G. Shi, S. Lei, Y. Zhang, S. Zhang, R. Vajtai, P.M. Ajayan, Direct laser-patterned micro-supercapacitors from paintable $MoS_2$ films, Small 9 (2013) 2905–2910, https://doi.org/10.1002/smll.201203164.

[57] K.C. Pham, D.S. McPhail, A.T.S. Wee, D.H.C. Chua, Amorphous molybdenum sulfide on graphene-carbon nanotube hybrids as supercapacitor electrode materials, RSC Adv. 7 (2017) 6856–6864, https://doi.org/10.1039/c6ra27901e.

[58] M.C.R. Kötz, Principles and applications of electrochemical capacitors, Electrochim. Acta 45 (2000) 2483–2498, https://doi.org/10.1016/S0013-4686(00)00354-6.

[59] A.H. Loo, A. Bonanni, Z. Sofer, M. Pumera, Exfoliated transition metal dichalcogenides ($MoS_2$, $MoSe_2$, $WS_2$, $WSe_2$): an electrochemical impedance spectroscopic investigation, Electrochem. Commun. 50 (2015) 39–42, https://doi.org/10.1016/j.elecom.2014.10.018.

[60] A. Ter Heijne, O. Schaetzle, S. Gimenez, F. Fabregat-Santiago, J. Bisquert, D.P.B.T.B. Strik, F. Barrière, C.J.N. Buisman, H.V.M. Hamelers, Identifying charge and mass transfer resistances of an oxygen reducing biocathode, Energy Environ. Sci. 4 (2011) 5035–5043, https://doi.org/10.1039/c1ee02131a.

[61] B.D. Boruah, A. Misra, Polyethylenimine mediated reduced graphene oxide based flexible paper for supercapacitor, Energy Storage Mater 5 (2016) 103–110, https://doi.org/10.1016/j.ensm.2016.05.007.

[62] S. Li, C. Yu, J. Yang, C. Zhao, M. Zhang, H. Huang, Z. Liu, W. Guo, J. Qiu, A superhydrophilic "nanoglue" for stabilizing metal hydroxides onto carbon materials for high-energy and ultralong-life asymmetric supercapacitors, Energy Environ. Sci. 10 (2017) 1958–1965, https://doi.org/10.1039/c7ee01040k.

[63] L.Q. Fan, Q.M. Tu, C.L. Geng, J.L. Huang, Y. Gu, J.M. Lin, Y.F. Huang, J.H. Wu, High energy density and low self-discharge of a quasi-solid-state supercapacitor with carbon nanotubes incorporated redox-active ionic liquid-based gel polymer electrolyte, Electrochim. Acta 331 (2020) 135425, https://doi.org/10.1016/j.electacta.2019.135425.